P18 Subsidence Evaluation

Rapport voor TAQA Energy BV

Fenix Consulting Delft BV
C.J. de Pater

Datum
October 2019

P18 Subsidence Evaluation

Rapport voor TAQA Energy BV

Datum
October 2019

Executive Summary

The P18 fields will induce seabed subsidence during depletion, which is almost complete. In the injection phase for CO2 storage, the seabed will rebound, which may only be partial since reservoir rocks often show less rebound compared with compaction during primary depletion.

The subsidence and uplift were computed with the so-called nucleus of strain method developed by Geertsma and Van Opstal. The subsidence evaluation uses the Eclipse grid and from each cell the contribution to total subsidence is added. The effect of a cell is proportional to compaction coefficient, pressure change and cell volume. The compaction coefficient has been computed from the Young's modulus used in the TNO design study of 18GPa and a Biot coefficient of 1.

Conclusions

- Subsidence at the platform during primary depletion is modest at 0.076m (7.6cm). The maximum subsidence is 0.101m (10.1cm).
- Rebound at the platform during CO2 injection is 0.076m (7.6cm) when pressure is restored to virgin pressure.
- For partial rebound due to hysteresis of reservoir stiffness, the uplift would be 0.03m (3cm) at virgin pressure.

Contents

List of Figures

List of Tables

Nomenclature

Units: SI (m= metre, s= second, kPa $=10^3$Pa, MPa $=10^6$Pa, GPa $=10^9$Pa)

Dimensions: m= mass, L= length, t= time

Variable		Description	Units	Dimensions
A_p	:	Poroelastic coefficient	[-]	(-)
E	:	Young's modulus	[GPa]	(m/Lt^2)
p	:	pressure	[MPa]	(m/Lt^2)
V_{res}	:	reservoir volume	[m^3]	(L^3)
α_B	:	Biot coefficient	[-]	(-)
ν	:	Poisson's ratio	[-]	(-)

1 Introduction

TAQA is planning (with PORTHOS partners) to use the depleted P18 fields for CO2 storage. The location of the fields and the various reservoir compartments are shown below, Figure 1.

The various compartments are indicated in the map of Figure 2. The P18-2 field consists of several compartments, while the P18-4 and P18-6 fields consist of a single compartment. The latter fields are isolated from the P18-2 field.
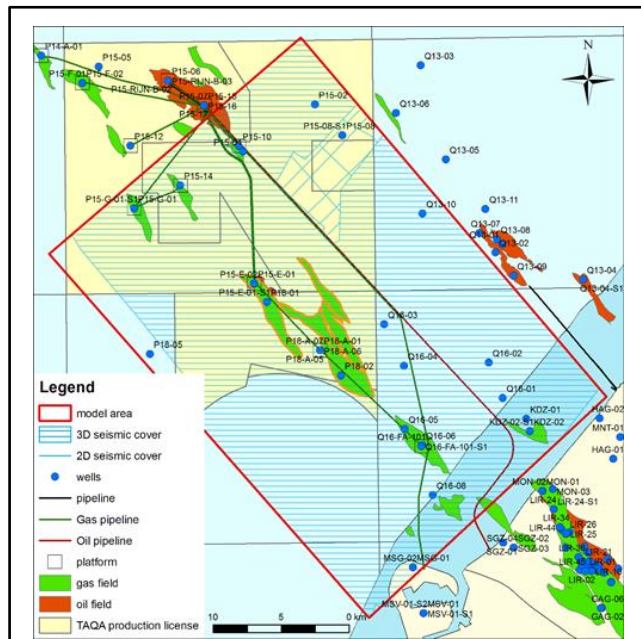
Figure 1: Overview of the locations of P15 and P18 fields (After TAQA, 2009).
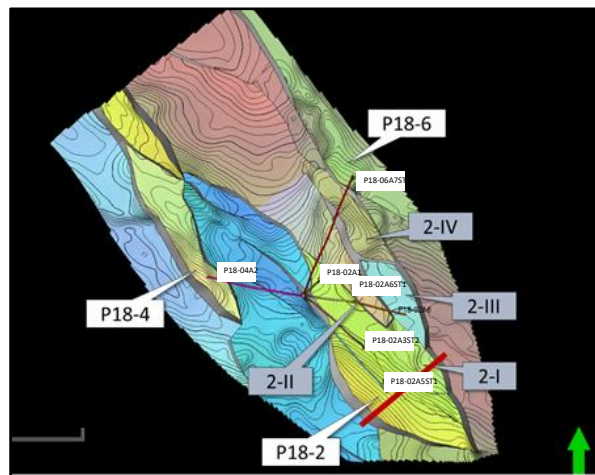
Figure 2: Overview of the three P18 fields (P18-2, P18-4, and P18-6), and the blocks of the P18-2 Field (2-I, 2-II, 2-III, and 2-IV). Red line indicates the position of the cross section shown in Figure 4. (TNO, 2019)

The reservoirs belong to the Triassic Buntsandstein and consist of the Hardegsen, Upper and Lower Detfurth and Volpriehausen. The tight Volpriehausen layer gives only a small contribution to the reservoir storage capacity. However, the full reservoir height of some 220m is included in the geomechanical analyses since these layers will all deplete or repressurize over time.

Figure 4 shows a typical cross-section through the P18-2 field with the bounding faults. The different compartments are shown in Figure 5, which will be used to select the compartments of the P18-2, P18-4 and P18-6 fields for the subsidence evaluation.
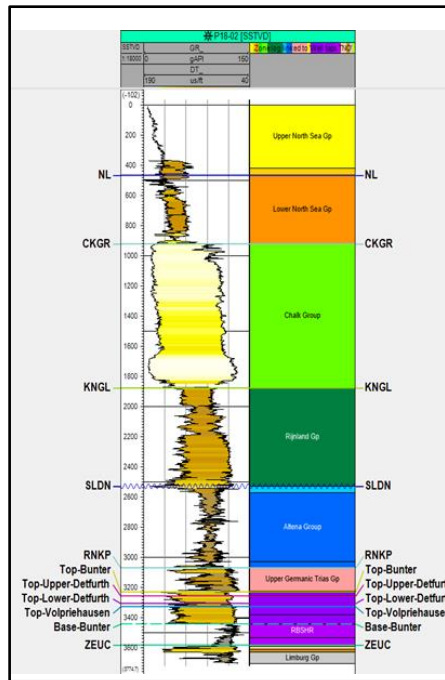
Figure 3: Lithology of the Triassic P18-2 field and overburden. The Hardegsen (Top Bunter) and Detfurth layers comprise the reservoir with a small contribution from the tight Volpriehausen layer. (TNO, 2019)
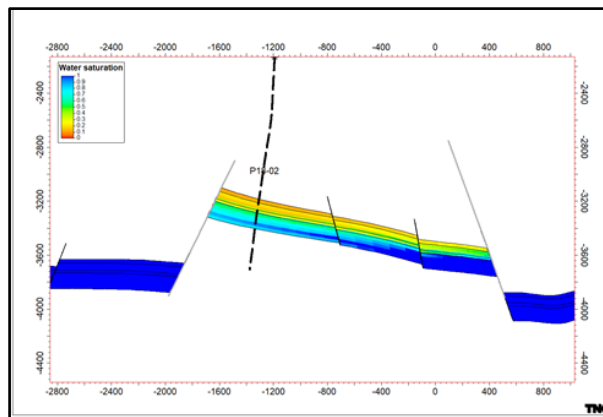
Figure 4: Cross section through the P18-2 field, showing block 2-I with initial water saturation. The location of the cross section is shown in Figure 2. (TNO, 2019)
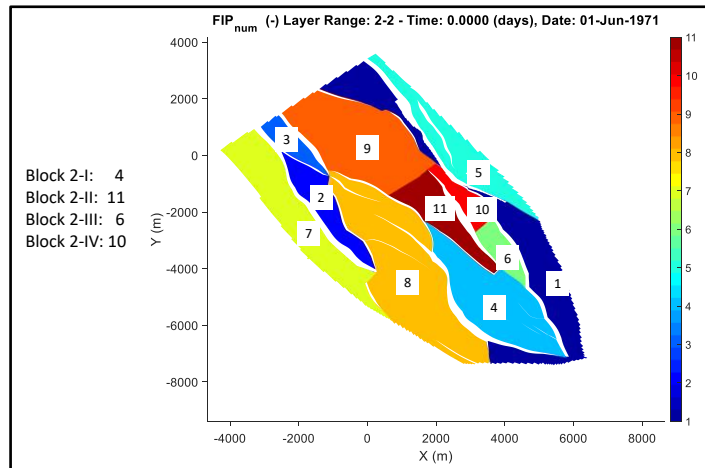
Figure 5: P18 Compartments with FIP numbers assigned to them.

2 Reservoir properties and pressure history

The Buntsandstein reservoirs are conventional gas reservoirs with fairly good porosity and permeability. The Young's modulus was determined from a dipole shear sonic log, shown in Figure 6. The average value of the modulus over the reservoir is 37GPa, assuming a ratio of static to dynamic modulus of 75%. We obtain a higher value of the modulus than used in the TNO study, but the lower estimate of 18 GPa will be used, which is equivalent to a conservative estimate of compaction. The reservoir properties are listed in Table 1.
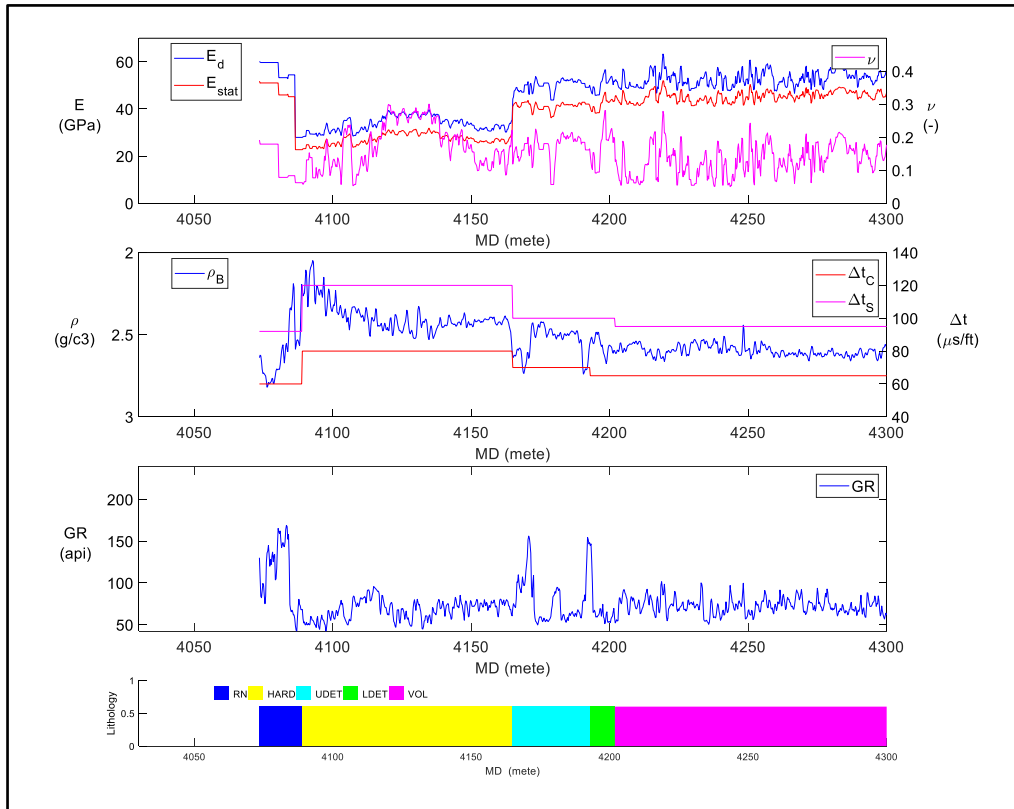
Figure 6: Logs and lithology in well P18-04A2. DSI readings from log displays were used to compute the modulus in overburden and reservoir.

**Table 1: Reservoir properties from TNO report (2019), except for stress which was determined from LOT and frac injections. Most properties apply to all three fields, but the pressure and stress changes apply to P18-2. The pressure for the other fields is listed in Table 2.**

Modulus			18	GPa	Virgin pressure	375	bar
Poisson ratio			0.25		Depleted pressure	20	bar
Biot Coefficient			1		Pressure drop	-355	bar
Compaction coefficient			0.046	1/GPa	Thermal expansion coefficient	1.00E-05	1/C
Depth			3500	m	Temperature drop	-90	C
Horizontal stress ratio			0.43		Thermal stress coefficient	2.4	bar/C
Stress path coefficient			0.60		Thermal stress drop	-216	bar
Vertical stress gradient			20.30	kPa/m	Poroelastic coefficient	0.67	
Minimum horizontal stress gradient			14.84	kPa/m	Poroelastic stress drop	-237	bar
Reservoir pressure gradient			10.71	kPa/m	Stress gradient drop	-6.8	kPa/m

3 Subsidence Calculation

Decreasing pressure causes higher effective stress on the reservoir rock so that the rock compacts. A fairly accurate estimate of the reservoir compaction can be obtained by summing the effect of a small volume of the reservoir over the entire reservoir volume (Geertsma, 1973).

For uniaxial compaction the reservoir height change is given by:

$$\Delta H_{res} = c_m \Delta p H_{res} \tag{1}$$

The surface deformation due to the pore pressure distribution in the reservoir can be calculated by summing the effect of a small volume of the reservoir over the entire reservoir volume. The small volume can be considered as a source (or nucleus) of strain. The surface subsidence can be written as:

$$u_z = \frac{c_m(1-\nu)}{\pi} \frac{d}{\left(r^2+d^2\right)^{3/2}} \Delta V \Delta p_{res} \quad c_m = \alpha_B \frac{(1+\nu)(1-2\nu)}{(1-\nu)E} \tag{2}$$

Where: d: depth, r: distance from nucleus, along the surface, c_m : compaction coefficient, ν : Poisson Ratio, Δp_{res} : reservoir pressure change, ΔV : volume of nucleus, α_B : Biot constant, E : Young's modulus. For a circular reservoir of height h the subsidence is given by:

$$u_z = 2c_m(1-\nu)h\Delta p_{res} \int_0^\infty e^{-\eta\alpha} J_0(u)J_1(\rho u)du \tag{3}$$

Where: $\eta = d/R$ and $\rho = r/R$, J_0 : Bessel function of order zero, , J_1 : Bessel function of order one.

Alternatively, Eqn 2 can also be directly used to compute subsidence from a pressure simulation. The pressure in each grid block is then used to compute its contribution to subsidence and the sum over all grid cells yields the total subsidence. This can also be done for each time step so that the subsidence (or uplift) is obtained over the course of reservoir recovery.

The method that Opstal developed to take into account the relative stiffness of the underburden was used to apply the nucleus of strain approach to subsidence. The semi-analytical method published by van Opstal was derived for a fixed Poisson Ratio of 0.25. The optimization of the coefficients for other values of the Poisson Ratio outlined in the paper by Van Opstal was used to generalize the computation for any value of the Poisson Ratio.

Table 2: Reservoir pressures per field.

	P18-2 (bar)	P18-4 (bar)	P18-6 (bar)
Initial pressure	375	340	377
End production / start injection pressure	20	20	45
90 hydrostatic pressure	316	290	321
100 hydrostatic pressure	351	322	357
Initial pressure	375	340	377

Results

Two Petrel models and an Eclipse model were provided from which the Eclipse grids of the reservoir were extracted:

- P18_TNO_2019-07-21 Stripped (2019-05-15).pet
- P18-6_reservoir(20190911)_clean4EBN.pet
- runL28_FC with CASEL6

Using the grid coordinates per cell, the cell volume was computed and the subsidence was computed over an area around the reservoirs. The first Petrel model contained only the P18-2 and P18-4 fields and the second Petrel model contained the P18-6 field and the Eclipse model contained the pressures computed for the depleted state. The latter pressure distribution was used to compute the reservoir compaction of P18-6.

For reservoir simulation some cells can be made inactive when they have low permeability or porosity. However, even tight layers will be depleted over time and contribute to compaction. So, the subsidence was computed for all cells in the reservoir grid and for the active cells. For P18-2 and P18-4 fields this gave a different result while P18-6 included all cells so only the results for all cells was computed. For P18-6 all cells were active, but the water leg is large and does not contribute to subsidence since it is very tight. So, for P18-6 one scenario is uniform pressure excluding the water leg, but the most accurate estimate is based on simulated pressures. It was found from reservoir simulation that the water bearing part of the Volpriehausen layer does not follow the gas pressure, so that should be excluded from the subsidence computation. All results are listed in Table 4, but the result that excluded the Volpriehausen water leg is plotted in the figures.

For the P18-2 field the subsidence contours are shown in Figure 7 for the scenario in that only excluded the water leg. Subsidence would be reversed for elastic behavior of the reservoir but it is generally observed that after compaction of rock, the rebound is much less due to inelastic behavior. For instance, in the Bergermeer gas storage only a partial rebound was observed after repressurization compared with initial subsidence.
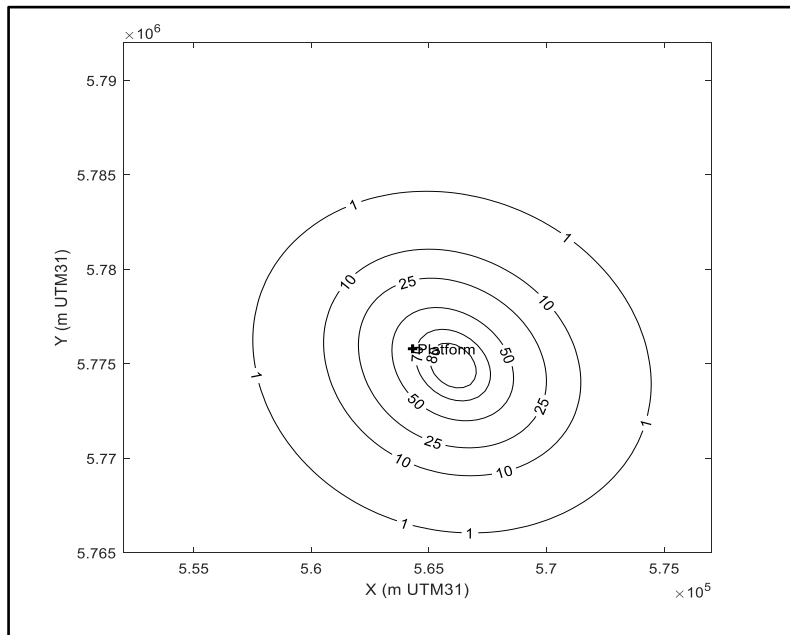
Figure 7: Maximum subsidence due to depletion of the P18-2 field.
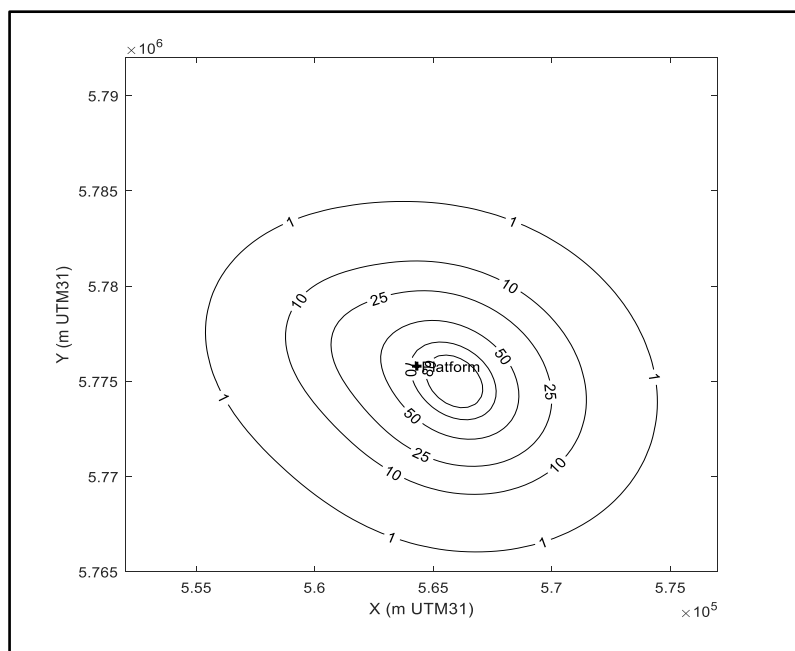
Figure 8: Maximum subsidence due to depletion of the P18-2 and P18-4 fields.
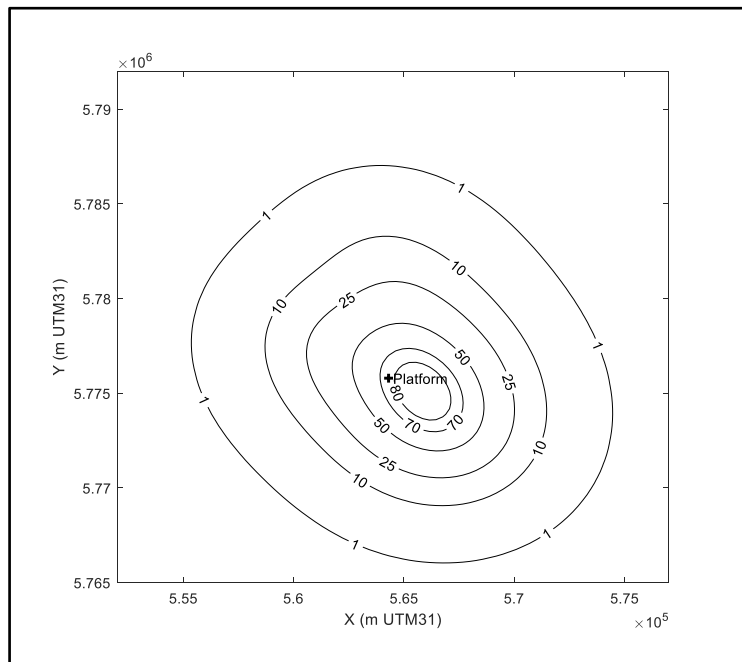
Figure 9: Maximum subsidence due to depletion of the P18-2, P18-4 and P18-6 fields.

Therefore, the rebound is given for elastic behavior, which would give a maximum uplift of 7.6cm. As a lower bound hysteresis would give an uplift of only 3cm, which corresponds with 2.5 times larger stiffness during rebound.
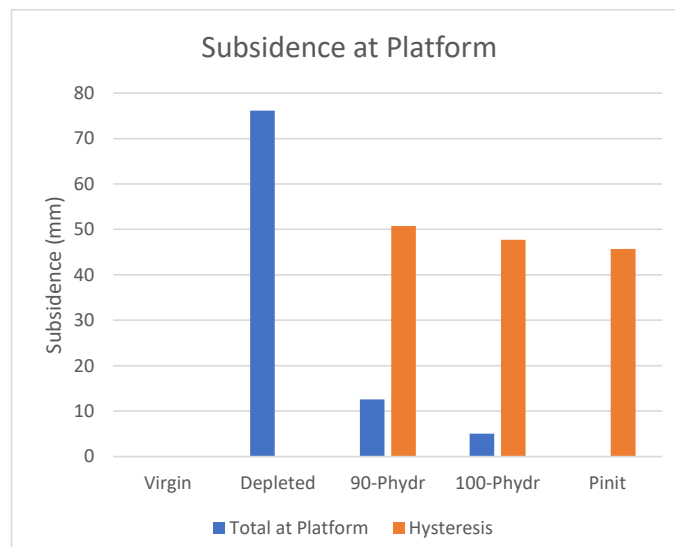
Figure 10: Subsidence at the platform location vs. depletion and repressurization of the P18-2, P18-4 and P18-6 fields. In the case of reservoir hysteresis only 40% of the compaction during depletion is recovered as rebound.
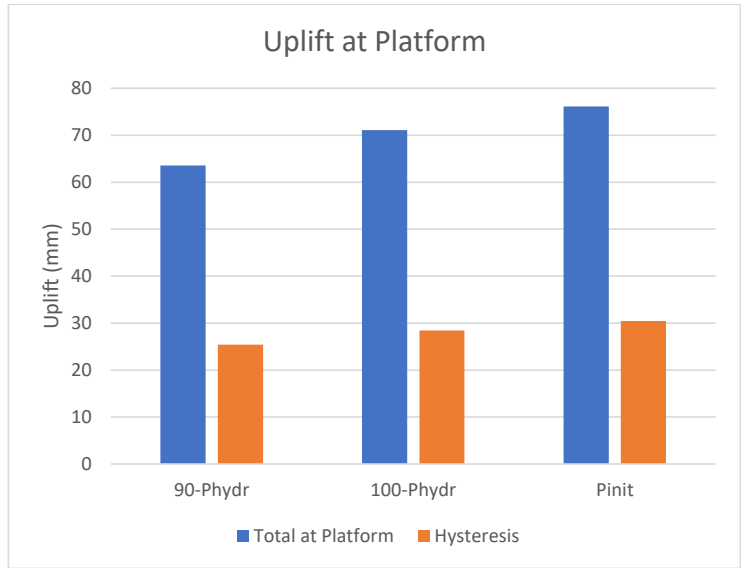
Figure 11: Uplift at the platform location vs. depletion and repressurization of the P18-2, P18-4 and P18-6 fields. In the case of reservoir stiffness hysteresis only 40% of the compaction during depletion is recovered as rebound.

Table 3: Total Subsidence and uplift (in mm) of platform as a function of pressure for the scenario that excluded only the water leg for P18-2 and P18-4. For P18-6 the simulated pressure was used.

	P18-2	P18-4	P18-6	Total at Platform	Hysteresis	Uplift Platform	Hysteresis
Initial pressure bar	375	340	377	0			
End production / start injection pressure bar	20	20	45	76			
90 hydrostatic pressure bar	316	290	321	13	60	64	16
100 hydrostatic pressure bar	351	322	357	5	58	71	18
Initial pressure bar	375	340	377	0	57	76	19

Table 4: Subsidence at the platform and maximum subsidence for different scenarios. Three different scenarios were computed: including all grid cells, only active cells and all cells excluding the Volpriehausen cells below the GWC were excluded. For P18-6 all cells were active, but the water leg is large and does not contribute to subsidence since it is very tight. So, for P18-6 one scenario is uniform pressure excluding the water leg, but the most accurate estimate is based on simulated pressure

	Scenario	Subsidence at platform (mm)	Maximum subsidence (mm)
P18-2	All cells	71	89
P18-2	Active	65	81
P18-2	NoWL	67	87
P18-4	All cells	10	26
P18-4	Active	9	24
P18-4	NoWL	7	16
P18-6	NoWL	4	11
P18-6	All cells-Psim	2	12
P18-2 & 4	All cells	81	93
P18-2 & 4	Active	74	84
P18-2 & 4	NoWL	74	89
P18-2 & 4 & 6	All Cells-No WL	76	101

References

Geertsma, J. and van Opstal, G. (1973). A Numerical Technique for Predicting Subsidence Above Compacting Reservoirs, Based on the Nucleus of Strain Concept. Verh. Kon. Ned. Geol. Mijnbouwk. Gen., 28, pp. 63-78.

TNO, (2019), "CO2 storage feasibility in the P18-2 depleted gas field", August 2019, TNO report 11111, Authors: Neele, F, T. Wildenborg, K. Geel, D. Loeve, L. Peters, S. Kahrobaei, T. Candela, M. Koenen, P.Hopmans, K. van der Valk, B. Orlic, V. Vandeweijer.